ACS APPLIED MATERIALS & INTERFACES

www.acsami.org

Forum Article

High-Performance Supercapacitor Electrodes Prepared From Dispersions of Tetrabenzonaphthalene-Based Conjugated Microporous Polymers and Carbon Nanotubes

Maha Mohamed Samy,[#] Mohamed Gamal Mohamed,[#] Ahmed. F. M. EL-Mahdy, Tharwat Hassan Mansoure, Kevin C.-W. Wu,* and Shiao-Wei Kuo*

Cite This: https://doi.org/10.1021/acsami.1c05720

Read Online

ACCESS | Metrics & More | Article Recommendations | Supporting Information

ABSTRACT: In this study, we prepared a series of conjugated microporous polymers (CMPs) through Sonogashira−Hagihara cross-couplings of a tetrabenzonaphthalene (TBN) monomer with pyrene (Py), tetraphenylethylene (TPE), and carbazole (Car) units and examined their chemical structures, thermal stabilities, morphologies, crystallinities, and porosities. TBN−TPE-CMP possessed a high surface area (1150 m^2 g^{-1}) and thermal stability (T_{d10} = 505 °C; char yield = 68 wt %) superior to those of TBN−Py-CMP and TBN−Car-CMP. To improve the conductivity of the TBN-CMP materials, we blended them with highly conductive single-walled carbon nanotubes (SWCNTs). Electrochemical measurements revealed that the TBN−Py-CMP/SWCNT nanocomposite had high capacitance (430 F g^{-1}) at a current density of 0.5 A g^{-1} and outstanding capacitance retention (99.18%) over 2000 cycles; these characteristics were superior to those of the TBN−TPE-CMP/SWCNT and TBN−Car-CMP/SWCNT nanocomposites.

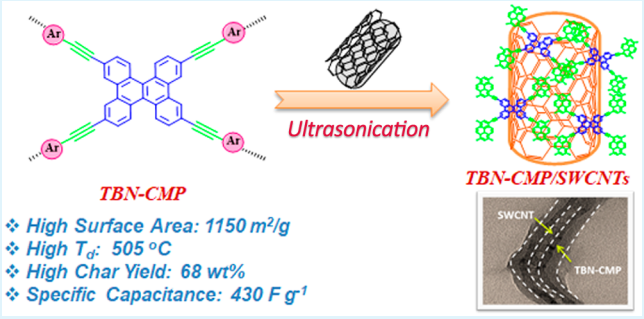

KEYWORDS: *conjugated microporous polymers, tetrabenzonaphthalene, carbon nanotubes, π−π-stacking interaction, supercapacitors*

INTRODUCTION

There is great demand at present to develop renewable energy systems to mitigate environmental deterioration resulting from the use of fossil fuels.[1−5] Supercapacitors are storage energy devices that function with characteristics between those of conventional capacitors and batteries. Energy storage in a supercapacitor occurs through electrostatic reactions between electrolyte ions and carbon electrodes. Supercapacitors are typically small in size and operate with large densities over wide temperature ranges, with rapid charge/discharge rates and outstanding cycle capacities.[6−9] Supercapacitors have already found applications industrially, particularly in electric trains and buses, cranes, elevators, and continuous power supply systems. The nature of the electrode materials plays an important role in determining the performance of a supercapacitor.[10] Many types of materials have been applied as supercapacitor electrodes, including hydroxides, electrochemically active organic molecules, metal oxides, carbon materials, and sulfides.[11−14] The use of inorganic materials as electrodes results in environmental pollution arising from their mining. Organic electroactive materials have become useful electrode materials for supercapacitors because of their flexibility, high sustainability, availability of resources, and environmental friendliness.[15,16]

Conjugated microporous polymers (CMPs) are a subclass of porous organic polymers that feature π-conjugation in their microporous frameworks. Because of the diverse types of available building blocks and reactions, CMP materials can be prepared with a wide range of structures and properties. For example, CMPs have been synthesized using common coupling reactions (e.g., Sonogashira−Hagihara, Suzuki−Miyaura, and Yamamoto coupling) as well as oxidative polymerization.[17−23] CMPs typically have many attractive characteristics: facile preparation, high surface area, porosity, strong activity toward visible light, high thermal stability, and good optoelectronic properties. As a result, CMPs are good candidates for use in such applications as energy storage, gas separation, metal ion sensing, production of solar fuels, gas adsorption, photocatalytic H_2 production, and photoredox catalysis.[4,24−41] Unfortunately, CMP materials have generally displayed low conductivity, decreasing their number of workable energy storage applica-

Special Issue: Emerging Materials for Catalysis and Energy Applications

Received: March 28, 2021
Accepted: April 28, 2021

Scheme 1. Synthesis of (a) TBN−Py-CMP, (b) TBN−TPE-CMP, and (c) TBN−Car-CMP

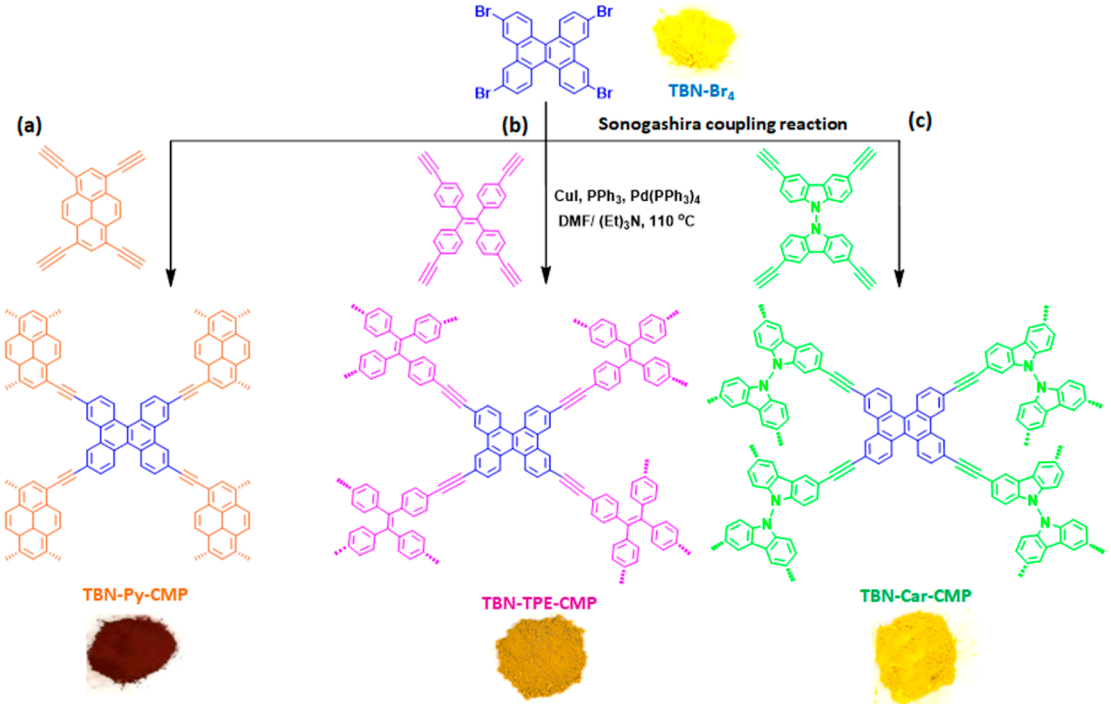

tions.[42−45] For example, Mohamed et al. found that a hyper-cross-linked porous organic polymer based on (4-(5,6-diphenyl-1*H*-benzimidazol-2-yl)triphenylamine (DPT) displayed a specific capacitance of 110 F g^{-1} at a current density of 0.5 A g^{-1};[6] they also reported two types of hyper-cross-linked porous organic polymers based on tetraphenylanthraquinone materials exhibiting capacitances at 0.2 A g^{-1} of 72.75 F g^{-1} for An-CPOP-1 and 98.40 F g^{-1} for An-CPOP-2, respectively.[46] Furthermore, Khattak et al. prepared a diaminopyridine (DAP)−1,3,5-triformylphloroglucinol (TFP) covalent organic framework (COF) displaying a capacitance of 98 F g^{-1} at 0.5 A g^{-1}.[47] In 2018, our group revealed that the specific capacitances at 0.2 A g^{-1} of TPA-COF-1, TPA-COF-2, TPA-COF-3, TPT-COF-4, TPT-COF-5, and TPT-COF-6 were 51.3, 14.4, 5.1, 2.4, 0.34, and 0.24 F g^{-1}, respectively.[48]

Carbon nanotubes (CNTs) are highly conductive carbon materials because of their unique structure and outstanding mechanical properties.[49,50] Most interestingly, CNT networks can function as flexible substrates for CMPs to create active flexible electrodes without the need for additives or binders, thereby facilitating electrode preparation.[51,52] Conductive carbon materials (e.g., CNTs, graphene, activated carbons) have been introduced to enhance the electrochemical performance of COFs, metal−organic frameworks (MOFs), and CMP matrices.[52−57] For example, Duan et al. reported CoPc-CMP/CNTs-2 nanocomposites displaying excellent capacity retention (89.2%) and a specific capacitance of 107.2 F g^{-1} at a current density of 10 A g^{-1}.[52] Lin et al. prepared a CNTs@Mn-MOF material displaying a specific capacitance (203.1 F g^{-1}) higher than that of the corresponding pure Mn-MOF (43.2 F g^{-1}).[57] Liu et al. found that TpPa-COF/single-walled CNT (SWCNT) hybrid materials displayed a specific capacitance of 153 F g^{-1} at 0.5 A g^{-1} as well as good cycling stability.[54]

We suspected that the blending of CNTs with tetrabenzonaphthalene (TBN)-based CMPs would be a useful method for constructing active electrodes for supercapacitors. In this report, we describe the preparation of three TBN-CMPs (TBN−Py-CMP, TBN−TPE-CMP, TBN−Car-CMP) through Sonogashira−Hagihara cross-couplings of a TBN building block with 1,3,6,8-tetraethynylpyrene (Py-T), 1,1,2,2-tetrakis(4-ethynylphenyl)ethene (TPE-T), and 3,3′,6,6′-tetraethynyl-9,9′-bicarbazole (Car-T) units, respectively, in *N*,*N*-dimethylformamide (DMF) and triethylamine (Et_3N) in the presence of tetrakis(triphenylphosphine)palladium(0) [$Pd(PPh_3)_4$] as the catalyst [Scheme 1]. We used Fourier transform infrared (FTIR) spectroscopy, solid-state ^{13}C nuclear magnetic resonance (NMR) spectroscopy, thermogravimetric analysis (TGA), scanning electron microscopy (SEM), transmission electron microscopy (TEM), the Brunauer−Emmett−Teller (BET) method, and X-ray diffraction to examine the chemical structures, morphologies, and properties of these TBN-CMP materials. We blended these TBN-CMPs with SWCNTs (2 wt %) to produce TBN-CMP/SWCNT nanocomposites stabilized through strong noncovalent interactions. TEM confirmed the dispersion of the SWCNTs within the TBN-CMP matrix. Gratifyingly, the electrochemical performance of the TBN-CMPs as electrode materials improved after their blending with the SWCNTs.

EXPERIMENTAL SECTION

Materials. Dichloromethane (DCM), trifluoromethanesulfonic acid (CF_3SO_3H), Et_3N, CuI, triphenylphosphine (PPh_3), and $Pd(PPh_3)_4$ were purchased from Sigma−Aldrich. Methanol and DMF were purchased from Acros. 1,3,6,8-Tetrabromopyrene (Py-Br_4), 3,3′,6,6′-tetrabromo-9,9′-bicarbazole (Car-Br_4), and tetrakis(4-bromophenyl)ethylene (TPE-Br_4) were synthesized using previously reported procedures.[4,6,41,58−61]

1,3,6,8-Tetrakis(2-(trimethylsilyl)ethynyl)pyrene (Py-TMS). A mixture of Py-Br_4 (1.00 g, 1.93 mmol), CuI (0.0590 g, 0.310 mmol), PPh_3 (0.122 g, 0.460 mmol), and $Pd(PPh_3)_4$ (0.110 g, 0.150 mmol) in toluene (14 mL) and Et_3N (14 mL) was stirred in a two-neck flask for 15 min. Ethynyltrimethylsilane (1.52 g, 15.5 mmol) was added, and then, the mixture was heated under reflux at 80 °C for 72 h. The

https://doi.org/10.1021/acsami.1c05720
ACS Appl. Mater. Interfaces XXXX, XXX, XXX−XXX

cooled mixture was filtered to remove any catalyst. After the toluene and Et_3N were removed from the reaction mixture by a rotary evaporator, the product residue was purified by extraction with DCM. The combined extracts were concentrated using a rotary evaporator. Methanol was added to the residue, forming a red precipitate (Py-TMS), which was filtered off and dried at 60 °C (0.85 g, 85%; Scheme S1). Temperature for onset of decomposition: 350 °C. FTIR (KBr, cm^{-1}, Figure S1): 3053 (aromatic C−H stretching), 2908 (aliphatic C−H stretching), 2100 (C≡C stretching), 1618 (C=C stretching). ^{1}H NMR (500 MHz, $CDCl_3$, δ, ppm, Figure S2): 0.413 (s, 36H, CH_3), 8.3 (s, 2H), 8.57 (s, 4H). ^{13}C NMR (600 MHz, $CDCl_3$, δ, ppm, Figure S3): 135.70, 132.40, 127.80, 119.20, 103.50, 101.60. (+)ESI-MS m/z 587.3 (calcd for $C_{36}H_{42}Si_4$) (Figure S4).

1,3,6,8-Tetraethynylpyrene (Py-T). A solution of Py-TMS (0.440 g, 0.820 mmol) and K_2CO_3 (0.900 g, 6.52 mmol) in anhydrous methanol (15 mL) was stirred at room temperature overnight. After filtration, the solution was concentrated to afford a brown solid (0.36 g, 94%; Scheme S1). Temperature for onset of decomposition: 350 °C. FTIR (KBr, cm^{-1}, Figure S5): 3279 (≡C−H), 3065 (aromatic C−H stretching), 2186 (C≡C stretching), 1618 (C=C stretching). ^{1}H NMR (500 MHz, $CDCl_3$, δ, ppm, Figure S6): 8.68 (s, 4H), 8.38 (s, 2H), 3.67 (s, 4H). ^{13}C NMR (125 MHz, $CDCl_3$, δ, ppm, Figure S7): 133.80, 130.80, 129.10, 127.80, 84.50, 59.70. (+)ESI-MS m/z 298.8 (calcd for $C_{24}H_{10}$) (Figure S8).

1,1,2,2-Tetrakis(4-((trimethylsilyl)ethynyl)phenyl)ethane (TPE-TMS). A mixture of TPE-Br_4 (1.00 g, 1.54 mmol), CuI (0.0470 g, 0.240 mmol), PPh_3 (0.100 g, 0.380 mmol), and $Pd(PPh_3)_4$ (0.0860 g, 0.120 mmol) in THF (14 mL) and Et_3N (14 mL) was stirred in a two-neck flask at 50 °C for 30 min. Ethynyltrimethylsilane (1.21 g, 12.3 mmol) was added dropwise, and then, the mixture was heated under reflux at 50 °C for 3 days. The resulting mixture was filtered and concentrated. The residue was purified through flash chromatography (SiO_2; DCM) to give a white powder (0.75 g, 75%; Scheme S1). Temperature for onset of decomposition: 200 °C. FTIR (KBr, cm^{-1}, Figure S9): 3060 (aromatic C−H stretching), 2920 (aliphatic C−H stretching), 2155 (C≡C stretching), 1618 (C=C stretching). ^{1}H NMR (500 MHz, $CDCl_3$, δ, ppm, Figure S10): 7.24 (d, J = 8.4 Hz, 8H), 6.88 (d, J = 8.4 Hz, 8H), 0.22 (s, 36H, CH_3). ^{13}C NMR (125 MHz, $CDCl_3$, δ, ppm, Figure S11): 144, 141, 132.7, 132, 122.3, 105.6, 95.8, 0.07. (+)ESI-MS m/z 717.4 (calcd for $C_{46}H_{52}Si_4$) (Figure S12).

1,1,2,2-Tetrakis(4-ethynylphenyl)ethene (TPE-T). A mixture of TPE-TMS (0.440 g, 0.650 mmol) and K_2CO_3 (0.900 g, 6.52 mmol) in methanol (10 mL) was stirred at room temperature overnight. The pale-yellow precipitate was filtered off and dried [0.37 g, 93%; Scheme S1]. T_m: 155.5 °C. FTIR (KBr, cm^{-1}, Figure S13): 3273 (≡C−H), 3042 (aromatic C−H stretching), 2109 (C≡C stretching), 1617 (C=C stretching). ^{1}H NMR (500 MHz, $CDCl_3$, δ, ppm, Figure S14): 7.24 (d, J = 8.4 Hz, 8H), 6.93 (d, J = 8.4 Hz, 8H), 3.06 (s, 4H, ≡C−H). ^{13}C NMR (125 MHz, $CDCl_3$, δ, ppm, Figure S15): 143.8, 141.6, 132.36, 132, 121.24, 83.6 (≡C−Ar), 77.88 (≡C−H). (+)ESI-MS m/z 428 (calcd for $C_{34}H_{20}$) (Figure S16).

3,3′,6,6′-Tetrakis((trimethylsilyl)ethynyl)-9,9′-bicarbazole (Car-TMS). A solution of Car-Br_4 (1.00 g, 1.54 mmol), PPh_3 (0.100 g, 0.380 mmol), and $Pd(PPh_3)_4$ (0.0860 g, 0.120 mmol) in THF (14 mL) and Et_3N (14 mL) was stirred in a two-neck flask at 50 °C for 30 min. Ethynyltrimethylsilane (1.21 g, 12.3 mmol) was added, and then, the mixture was heated under reflux at 50 °C for 3 days. The resulting solution was filtrated to remove any catalyst and concentrated. The residue was purified through flash chromatography (SiO_2; DCM) to give a white powder (0.89 g, 89%, Scheme S1). T_m: 130 °C. FTIR (KBr, cm^{-1}, Figure S17): 3060 (aromatic C−H stretching), 2920 (aliphatic C−H stretching), 2155 (C≡C stretching), 1618 (C=C stretching), 1284 (C−N stretching). ^{1}H NMR (500 MHz, $CDCl_3$, δ, ppm, Figure S18): 8.31 (s, 4H), 7.47 (d, 4H), 6.75 (d, 4H), 0.31 (s, 36H, CH_3). ^{13}C NMR (125 MHz, $CDCl_3$, δ, ppm, Figure S19): 140.33, 132.13, 126.21, 122.56, 117.55, 109.8, 105.7, 93.86. (+)ESI-MS m/z 717.2 (calcd for $C_{44}H_{88}N_2Si_4$) (Figure S20).

3,3′,6,6′-Tetraethynyl-9,9′-bicarbazole (Car-T). A solution of Car-TMS (0.440 g, 0.650 mmol) and K_2CO_3 (0.900 g, 6.52 mmol) in methanol (10 mL) was stirred at room temperature for 12 h. The pale-yellow precipitate was filtered off and dried (0.35 g, 80%, Scheme S1). Temperature for onset of decomposition: 180 °C. FTIR (KBr, cm^{-1}, Figure S21): 3285 (≡C−H), 3065 (aromatic C−H stretching), 2105 (C≡C stretching), 1620 (C=C stretching), 1286 (C−N stretching). ^{1}H NMR (500 MHz, $CDCl_3$, δ, ppm, Figure S22): 8.32 (s, 4H), 7.51 (d, 4H), 6.84 (d, 4H), 3.09 (s, 4H, ≡C−H). ^{13}C NMR (125 MHz, $CDCl_3$, δ, ppm, Figure S23): 140.24, 132.02, 125.61, 122.24, 116.61, 109.77, 84.33 (≡C−Ar), 76.67 (≡C−H). (+)ESI-MS m/z 428 (calcd for $C_{32}H_{16}N_2$) (Figure S24).

2,7,10,15-Tetrabromotetrabenzonaphthalene (TBN-Br_4). In a two-neck flask under a N_2 atmosphere, TPE-Br_4 (3.00 g, 4.60 mmol) was added to dry DCM (230 mL), and then, the flask was cooled in ice for 1 h. CF_3SO_3H (2.76 mL) was added slowly; the resulting mixture was stirred for 1 h at 0 °C and then at ambient temperature for 4 h. Methanol (50 mL) was poured into the flask, and then, the mixture was stirred at ambient temperature overnight. The precipitate was filtered off and washed many times with THF, methanol, and acetone to give a pale brown solid (1.85 g, 62%). T_m > 300 °C. FTIR (KBr, cm^{-1}, Figure S25): 3079 (aromatic C−H stretching), 566 (C−Br stretching). ^{1}H NMR (500 MHz, $CDCl_3$, δ, ppm, Figure S26): 8.76 (d, 4H), 8.42 (d, 4H), 7.74 (dd, 4H). ^{13}C NMR spectrum of TBN-Br_4 could not be provided for this compound because of its poor solubility in organic solvents. (+)ESI-MS m/z 644.1 (calcd for $C_{26}H_{12}Br_4$) (Figure S27).

TBN−Py-CMP. A solution of TBN-Br_4 (140 mg, 0.220 mmol), Py-T (100 mg, 0.330 mmol), CuI (4.00 mg, 0.0200 mmol), PPh_3 (5.60 mg, 0.0200 mmol), and $Pd(PPh_3)_4$ (20.0 mg, 0.0200 mmol) was heated in DMF (5 mL) and Et_3N (5 mL) at 110 °C for 3 days. The resulting precipitate was filtered off and washed well with THF, methanol, and acetone. The solid was dried in an oven under vacuum at 100 °C overnight to give a deep-red solid (0.19 g, 73%). FTIR (KBr, cm^{-1}): 3051 (C−H aromatic), 2197 (C≡C), 1635 (C=C).

TBN−TPE-CMP. A solution of TBN-Br_4 (100 mg, 0.150 mmol), TPE-T (100 mg, 0.230 mmol), CuI (3.00 mg, 0.0150 mmol), PPh_3 (4.00 mg, 0.015 mmol), and $Pd(PPh_3)_4$ (20.0 mg, 0.0150 mmol) in DMF (5 mL) and Et_3N (5 mL) was heated under reflux at 110 °C for 72 h. After cooling, the precipitate was filtered off, washed many times with THF, methanol, and acetone, and dried to afford a yellow solid (0.23 g, 85%). FTIR (KBr, cm^{-1}): 3075 (C−H aromatic), 2199 (C≡C), 1635 (C=C).

TBN−Car-CMP. A solution of TBN-Br_4 (100 mg, 0.150 mmol), 3,3′,6,6′-tetraethynyl-9,9′-bicarbazole (100 mg, 0.230 mmol), CuI (3.00 mg, 0.0150 mmol), PPh_3 (4.00 mg, 0.0150 mmol), and $Pd(PPh_3)_4$ (20.0 mg, 0.0150 mmol) in DMF (5 mL) and Et_3N (5 mL) was heated under reflux at 110 °C for 72 h. The yellow precipitate was filtered off; washed thoroughly with THF, MeOH, and acetone; and dried (0.22 g, 81%). FTIR (KBr, cm^{-1}): 3063 (C−H aromatic), 2202 (C≡C), 1617 (C = C).

TBN-CMP/SWCNT Nanocomposites. A mixture of a TBN-CMP monomer and an SWCNT (2 wt %) in THF was sonicated at room temperature for 10 h. The solvent was evaporated at 60 °C over 24 h in an oven. The resulting TBN-CMP/SWCNT (2 wt % SWCNT) nanocomposite was imaged using TEM (Scheme 2).

RESULTS AND DISCUSSION

Synthesis of TBN−Py-CMP, TBN−TPE-CMP, and TBN−Car-CMP. Scheme 1 displays our schematic route for the preparation of the three types of TBN-CMPs, through Sonogashira couplings of TBN-Br_4 with Py-T, TPE-T, and Car-T, respectively, in a mixture of DMF and Et_3N (1:1) in the presence of a palladium catalyst. All of the resultant CMP polymers were insoluble in most common solvents. The chemical structures of these three microporous polymers were confirmed using FTIR spectroscopy and solid-state NMR spectroscopy. FTIR spectra [Figure 1(A)] confirmed the presence of the alkyne linkers of the three conjugated polymers through the appearance of a stretching absorption band for −C≡C− bonds near 2200 cm^{-1}. In addition, absorption bands at 3075−3051 and 1628 cm^{-1} appeared in the FTIR spectra of

https://doi.org/10.1021/acsami.1c05720
ACS Appl. Mater. Interfaces XXXX, XXX, XXX−XXX

Scheme 2. (a) Blending TBN-CMP with SWCNT in THF Solution, (b) Ultrasonication of TBN-CMP with SWCNT in THF Solution, (c) Formation of TBN-CMP/SWCNT Nanocomposites through $\pi-\pi$-Stacking, and (d) TEM Images of TBN-CMP/SWCNT

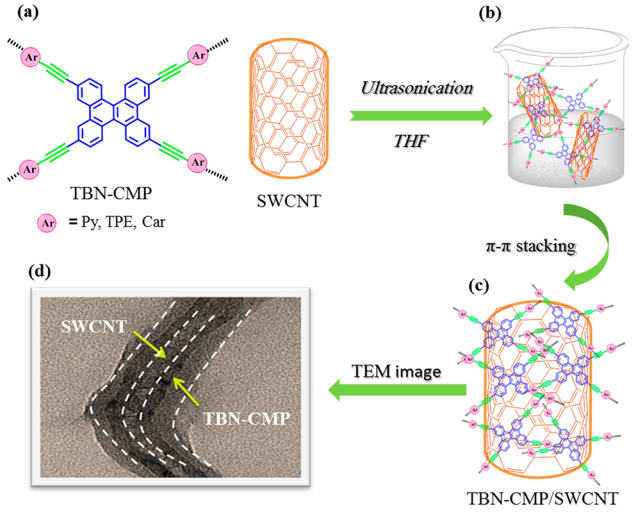

these three polymers, representing the stretching of aromatic C−H and C=C units. Figure 1(B) presents the solid-state ^{13}C NMR spectra of TBN−Py-CMP, TBN−TPE-CMP, and TBN−Car-CMP, recorded at room temperature. The signals of the aromatic carbon nuclei in these frameworks appeared in the range of 121−139 ppm, with signals at 78 ppm representing their alkyne groups. The spectrum of TBN−TPE-CMP [Figure 1B-(b)] featured an additional peak at 141 ppm, representing the ethylene group in the TPE unit. TGA [Figure 1(C) and Table 1] revealed that all three TBN-CMPs were stable under

Table 1. Thermal Stabilities and Porosity Properties of TBN−Py-CMP, TBN−TPE-CMP, and TBN−Car-CMP

sample	T_{d5} (°C)	T_{d10} (°C)	char yield (wt %)	surface area (m^2/g)	pore size (nm)
TBN−Py-CMP	343	439	58	473	1.05
TBN−TPE-CMP	405	505	68	1150	1.07
TBN−Car-CMP	380	480	54	762	1.04, 2

N_2 at temperatures of up to 430 °C, with the 10% weight losses for TBN−Py-CMP, TBN−TPE-CMP, and TBN−Car-CMP occurring at 439, 505, and 480 °C, respectively, along with char yields of 58, 67, and 54 wt %, respectively. All of the prepared CMPs had amorphous structures, with no crystalline diffraction peaks appearing in their X-ray diffraction patterns [Figure 1(D)], consistent with other reported microporous networks.[61,62]

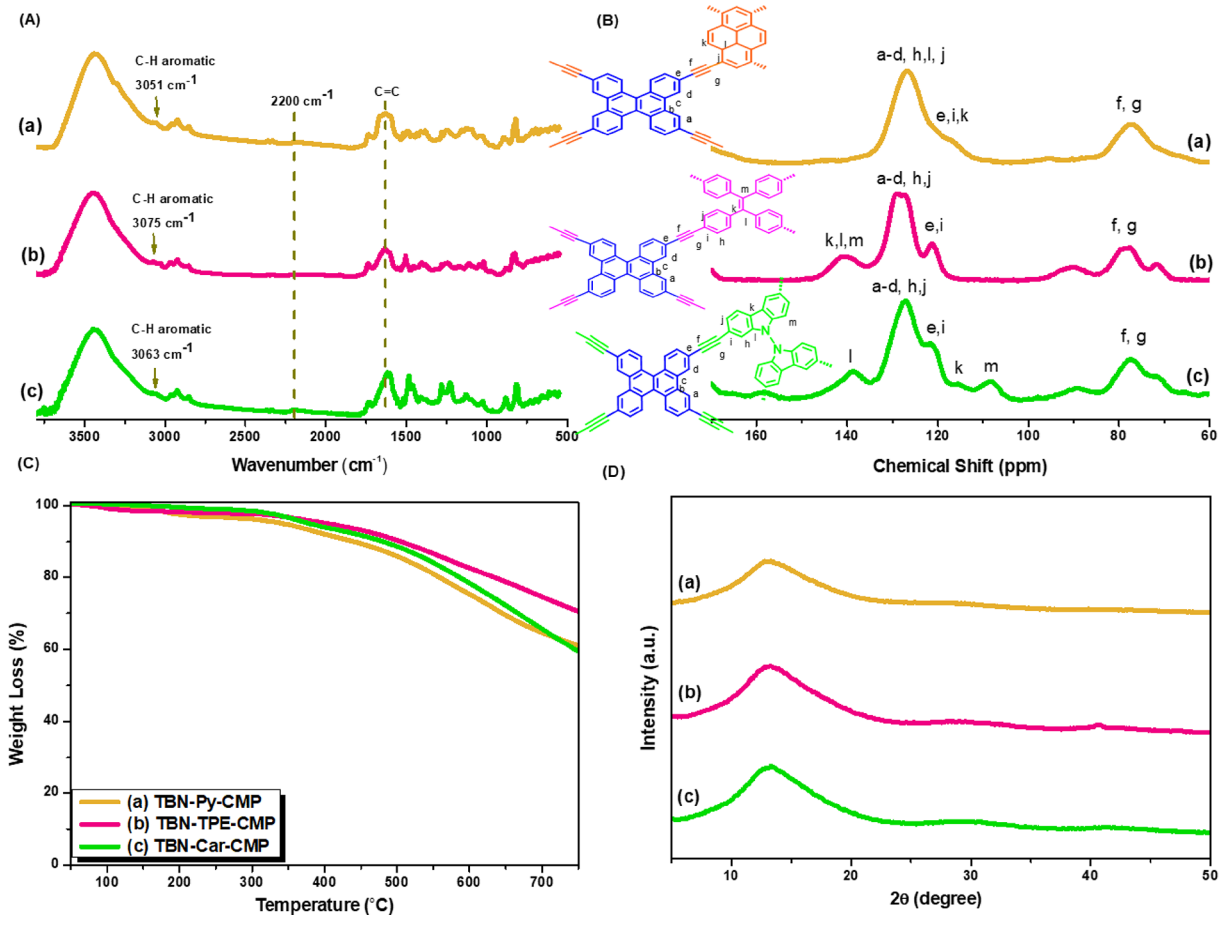

Figure 1. (A) FTIR spectra of (a) TBN-Py-CMP, (b) TBN-TPE-CMP, and (C) TBN-Car-CMP, recorded at 25 °C. (B) ^{13}C NMR spectra of (a) TBN-Py-CMP, (b) TBN-TPE-CMP, and (c) TBN-Car-CMP. (C) TGA curves of (a) TBN-Py-CMP, (b) TBN-TPE-CMP, and (c) TBN-Car-CMP. (D) XRD profiles of (a) TBN-Py-CMP, (b) TBN-TPE-CMP, and (c) TBN-Car-CMP.

https://doi.org/10.1021/acsami.1c05720
ACS Appl. Mater. Interfaces XXXX, XXX, XXX−XXX

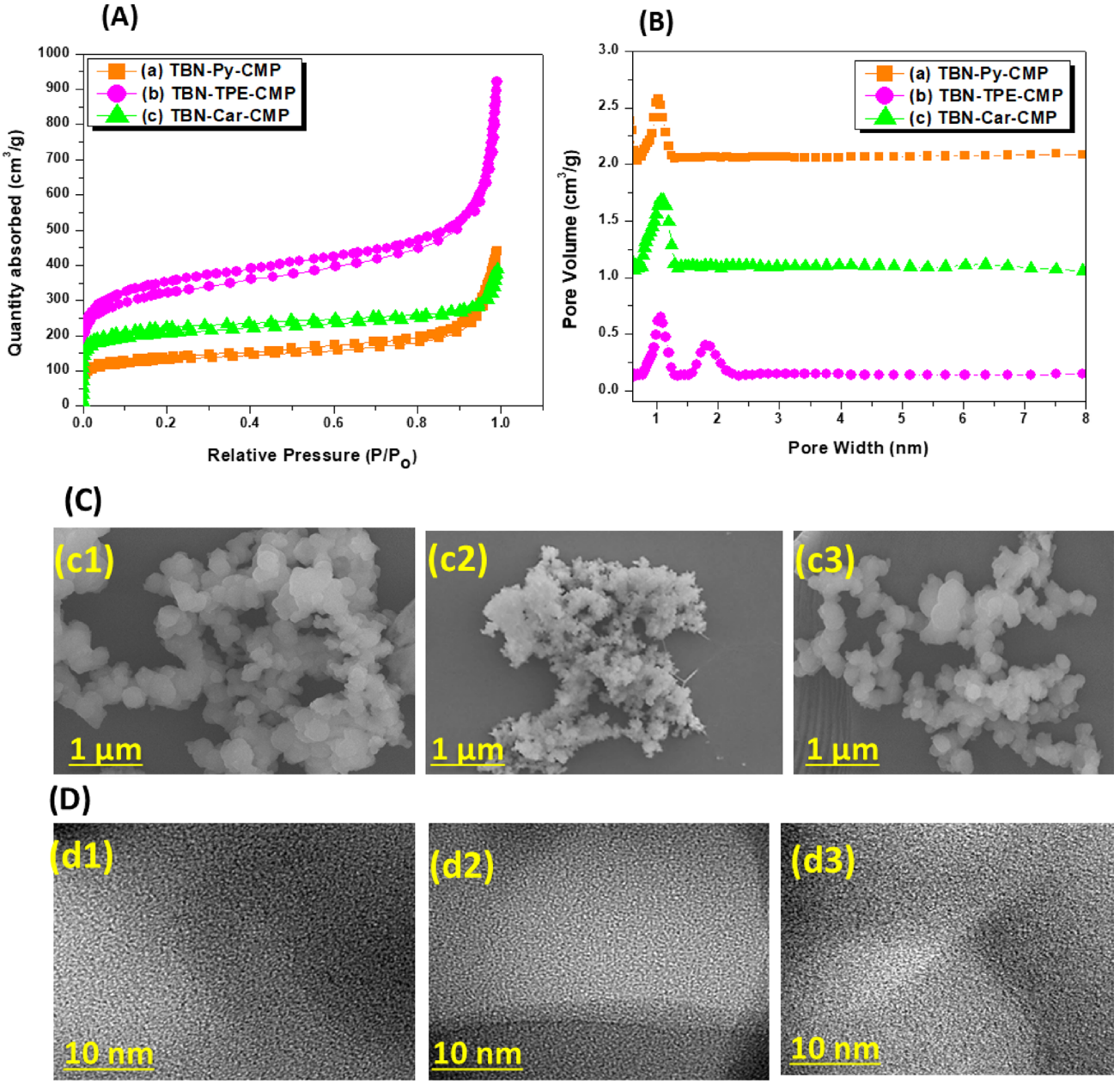

Figure 2. (A) N_2 adsorption/desorption isotherms of (a) TBN-Py-CMP, (b) TBN-TPE-CMP, and (c) TBN-Car-CMP. (B) Pore size distribution curves of (a) TBN-Py-CMP, (b) TBN-TPE-CMP, and (c) TBN-Car-CMP. (C) SEM images of (c1) TBN-Py-CMP, (c2) TBN-TPE-CMP, and (c3) TBN-Car-CMP. (D) TEM images of (d1) TBN-Py-CMP, (d2) TBN-TPE-CMP, and (d3) TBN-Car-CMP.

To determine the porosities of the three TBN-CMPs, we examined their N_2 sorption behavior at 77 K. As illustrated in Figure 2(A), the three CMPs all provided type II isotherms with a sharp increase in the lower P/P_0 region (<0.02). This behavior confirmed that the surfaces of these materials featured substantial micropores, with specific surface areas and total pore volumes (at $P/P_0 = 0.99$) of 473 $m^2\ g^{-1}$ and 0.678 $cm^3\ g^{-1}$, respectively, for TBN−Py-CMP; 1150 $m^2\ g^{-1}$ and 1.426 $cm^3\ g^{-1}$, respectively, for TBN−TPE-CMP; and 762 $m^2\ g^{-1}$ and 0.600 $cm^3\ g^{-1}$, respectively, for TBN−Car-CMP. Furthermore, we used nonlocal density functional theory (NLDFT) to estimate the pore sizes of these three CMPs from their N_2 sorption isotherms. The pore size distribution (PSD) curves [Figure 2(B)] revealed that TBN−Py-CMP and TBN−Car-CMP possessed micropores (average diameters: 1.05 and 1.07 nm, respectively), whereas TBN−TPE-CMP possessed both micropores and lower mesopores (average diameters of 1.04 and 2.00 nm, respectively). Furthermore, SEM imaging [Figure 2(C) revealed that the TBN-CMPs featured aggregated small particles with diameters of less than 20 nm. TEM images [Figure 2(D)] showed that the TBN-CMPs featured microporous structures.

Figure 3 displays photographs of the pure SWCNTs, solutions of the pure TBN-CMPs in THF, and the TBN-CMP/SWCNT nanocomposites. The SWCNTs formed a precipitate in THF [Figure 3(a2)], confirmed by the TEM image in Figure 3(a). All of the TBN-CMPs formed clear solutions in THF [Figure 3(b1,c1,d1)]; the addition of TBN-CMPs to the SWCNTs led to dissolving of the nanotubes [Figure 3(b2,c2,d2)], indicating that noncovalent interactions ($\pi-\pi$-stacking) occurred between

https://doi.org/10.1021/acsami.1c05720
ACS Appl. Mater. Interfaces XXXX, XXX, XXX−XXX

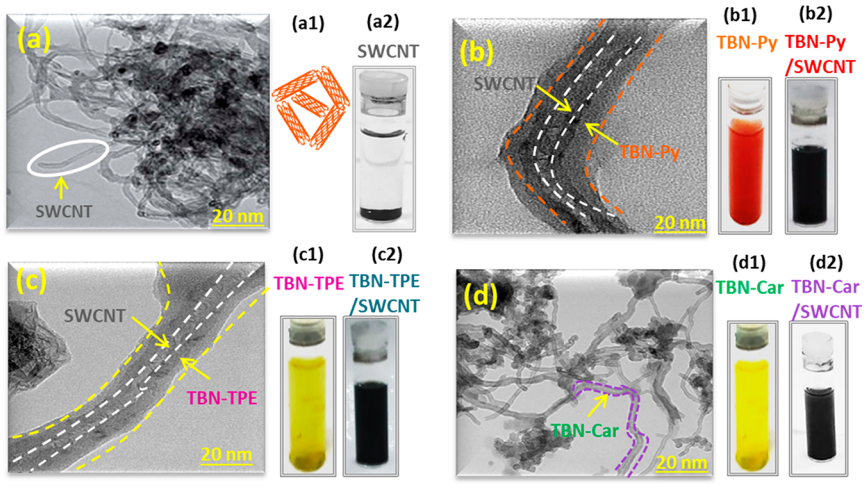

Figure 3. TEM images of (a) the pure SWCNTs and the (b) TBN−Py-CMP/SWCNT, (c) TBN−TPE-CMP/SWCNT, and (d) TBN−Car-CMP/SWCNT composites. Photographs of (a1,a2) the pure SWCNTs, (b1) TBN−Py-CMP, (b2) the TBN−Py-CMP/SWCNT complex, (c1) TBN-TBE-CMP, (c2) the TBN−TPE-CMP/SWCNT complex, (d1) TBN−Car-CMP, and (d2) the TBN−Car-CMP/SWCNT complex.

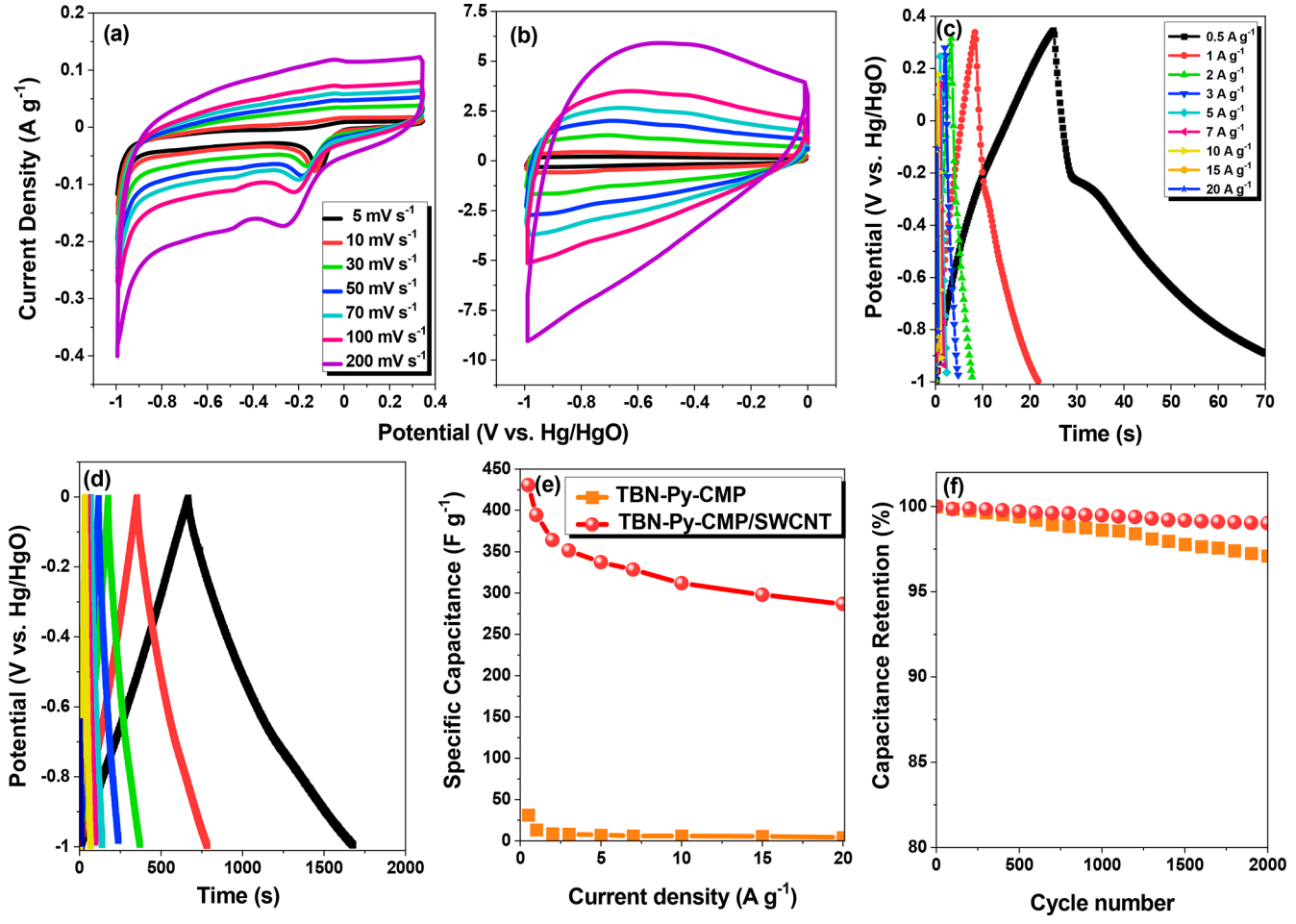

Figure 4. (a,b) CV curves of (a) TBN−Py-CMP and (b) the TBN−Py-CMP/SWCNT composite. (c,d) GCD curves of (c) TBN−Py-CMP and (d) the TBN−Py-CMP/SWCNT composite, measured at various currents. (e) Specific capacitances of TBN−Py-CMP and the TBN−Py-CMP/SWCNT composite, measured at current densities from 0.5 to 20 A g^{-1}. (f) Cycling stabilities of TBN−Py-CMP and the TBN−Py-CMP/SWCNT composite, measured at 10 A g^{-1} over 2000 cycles.

the TBN-CMPs and SWCNTs, forming soluble complexes. The TEM images in Figure 3(b−d) confirmed the uniform dispersion of the SWCNTs (2 wt %) in the TBN-CMP matrices. TGA [Figure S28 and Table S1] showed that the 10% weight losses for TBN−Py-CMP/SWCNT, TBN−TPE-CMP/SWCNT, and TBN−Car-CMP/SWCNT occurring at 306, 198.50, and 274.50 °C, respectively, along with char yields of 57.54, 42.04, and 50 wt %, respectively.

https://doi.org/10.1021/acsami.1c05720
ACS Appl. Mater. Interfaces XXXX, XXX, XXX−XXX

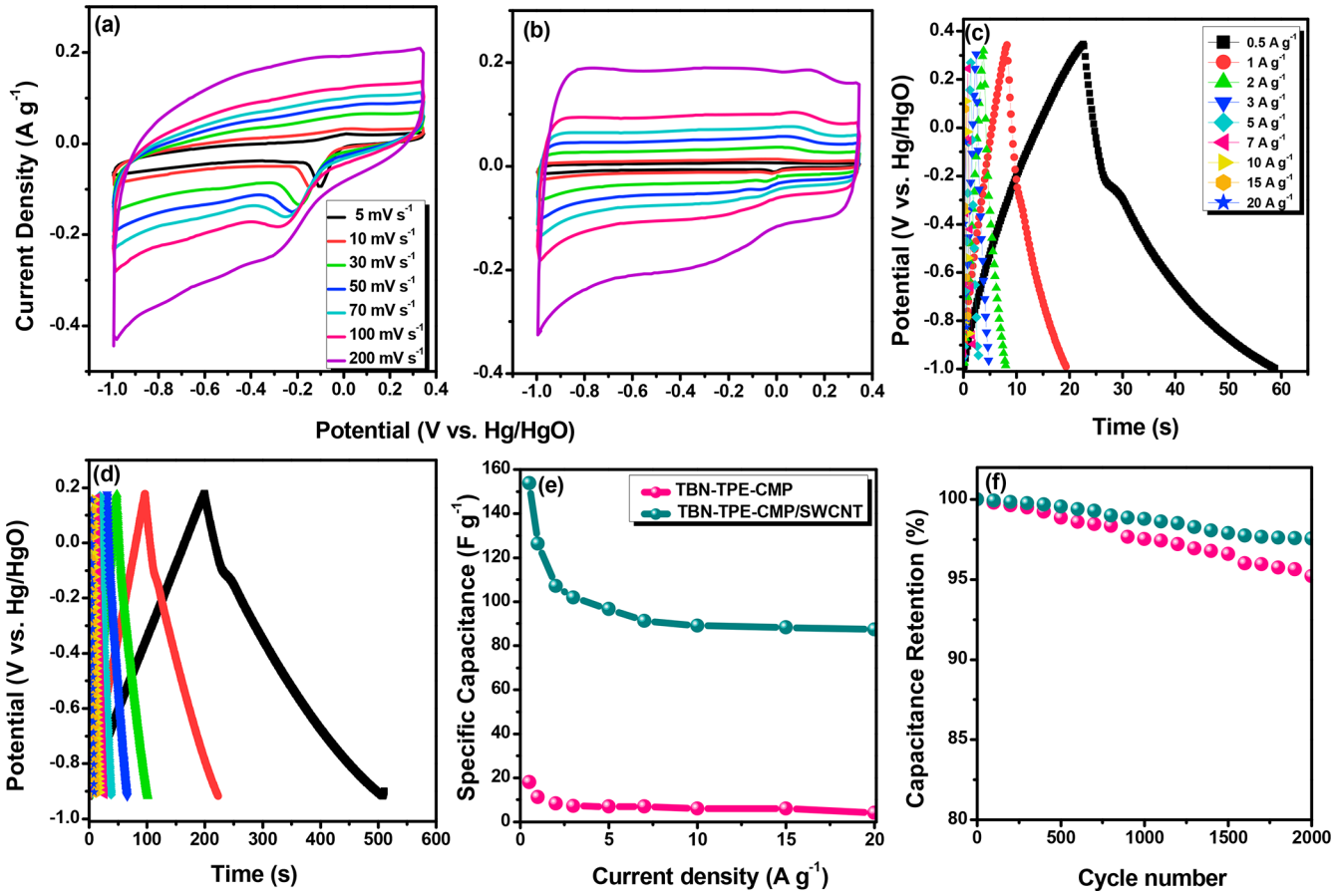

Figure 5. (a,b) CV profiles of (a) TBN−TPE-CMP and (b) the TBN−TPE-CMP/SWCNT composite. (c,d) GCD profiles of (c) TBN−TPE-CMP and (d) the TBN−TPE-CMP/SWCNT composite, measured at various currents. (e) Specific capacitances of TBN−TPE-CMP and the TBN−TPE-CMP/SWCNT composite, measured at current densities from 0.5 to 20 A g^{-1}. (f) Cycling stabilities of TBN−TPE-CMP and the TBN−TPE-CMP/SWCNT composite, measured at 10 A g^{-1} over 2000 cycles.

Electrochemical Performance. We estimated the electrochemical performance of the three TBN-CMPs and their composites with the SWCNTs through cyclic voltammetry (CV) and galvanostatic charge−discharge (GCD) measurements in a three-electrode system with 1 M aqueous KOH as the electrolyte. We compared the CV profiles of all of the TBN-CMPs and TBN-CMP/SWCNT materials at various sweep rates from 5 to 200 mV s^{-1} [Figures 4(a,b), 5(a,b), and S29(a,b)]. The corresponding CV curves of all of the TBN-CMP and TBN-CMP/SWCNT samples had rectangular shapes featuring humps, indicating that their capacitive responses originated from electric double-layer capacitance (EDLC).[4,6] The distinct appearance of humps in the rectangular shapes was indicative of pseudocapacitance arising from the presence of the nitrogen heteroatoms (in the case of TBN−Car-CMP) and electron-rich phenyl rings, for which reversible radical redox processes occurred during charge and discharge processes.[63] In addition, the current density increased upon increasing the sweep rate from 5 to 200 mV s^{-1} while retaining the shape of the CV curves, indicating good rate capability and facile kinetics.[47] The GCD measurements of all of the TBN-CMPs and TBN-CMP/SWCNT samples were performed at current densities varying from 0.5 to 20 A g^{-1} [Figures 4(c,d), 5(c,d), and S29(c,d)]. These GCD curves had triangular shapes featuring a slight bend, suggesting both pseudocapacity and EDLC characteristics.[49] The discharging times of the TBN-CMP/SWCNT materials were longer than those of the TBN-CMPs, indicating that the capacitance of the TBN-CMP materials was significantly improved after combining them with the SWCNTs. We estimated the specific capacitances of the TBN-CMP and TBN-CMP/SWCNT materials from their GCD curves. At a current density of 0.5 A g^{-1}, the specific capacitances of the TBN−Py-CMP, TBN−TPE-CMP, TBN−Car-CMP, TBN−Py-CMP/SWCNT, TBN−TPE-CMP/SWCNT, and TBN−Car-CMP/SWCNT materials were 31, 18.45, 18.90, 430, 156, and 53 F g^{-1}, respectively [Figures 4(e), 5(e), and S29(e)]. For comparison, Li et al. synthesized a series of nanostructured pyrene/graphene composites (PGCs)[64] and found that the optimized PGC electrode exhibited a specific capacitance of 310.7 F g^{-1} at a current density of 1.5 A g^{-1} as well as excellent cycle stability (capacitance retention of 99% after 15 000 cycles). They attributed this excellent performance to the high electrochemical activity of pyrene, the highly conductive and porous structure, and the improved wettability between the electrode and electrolyte. Therefore, decoration with pyrene can improve the hydrophilicity of an SWCNT surface, with the hydrophilic characteristics offering spaces for ready access of electrolyte ions, leading to rapid mass transport and enhanced electrochemical performance.[64]

In addition, the porous structure of an SWCNT provides diffusion channels and more efficient transport of electrolyte ions, thereby improving the capacitance. We examined the cyclic stability of our CMPs, before and after their blending with the SWCNTs, at a current density of 10 A g^{-1}. The capacitance

https://doi.org/10.1021/acsami.1c05720
ACS Appl. Mater. Interfaces XXXX, XXX, XXX−XXX

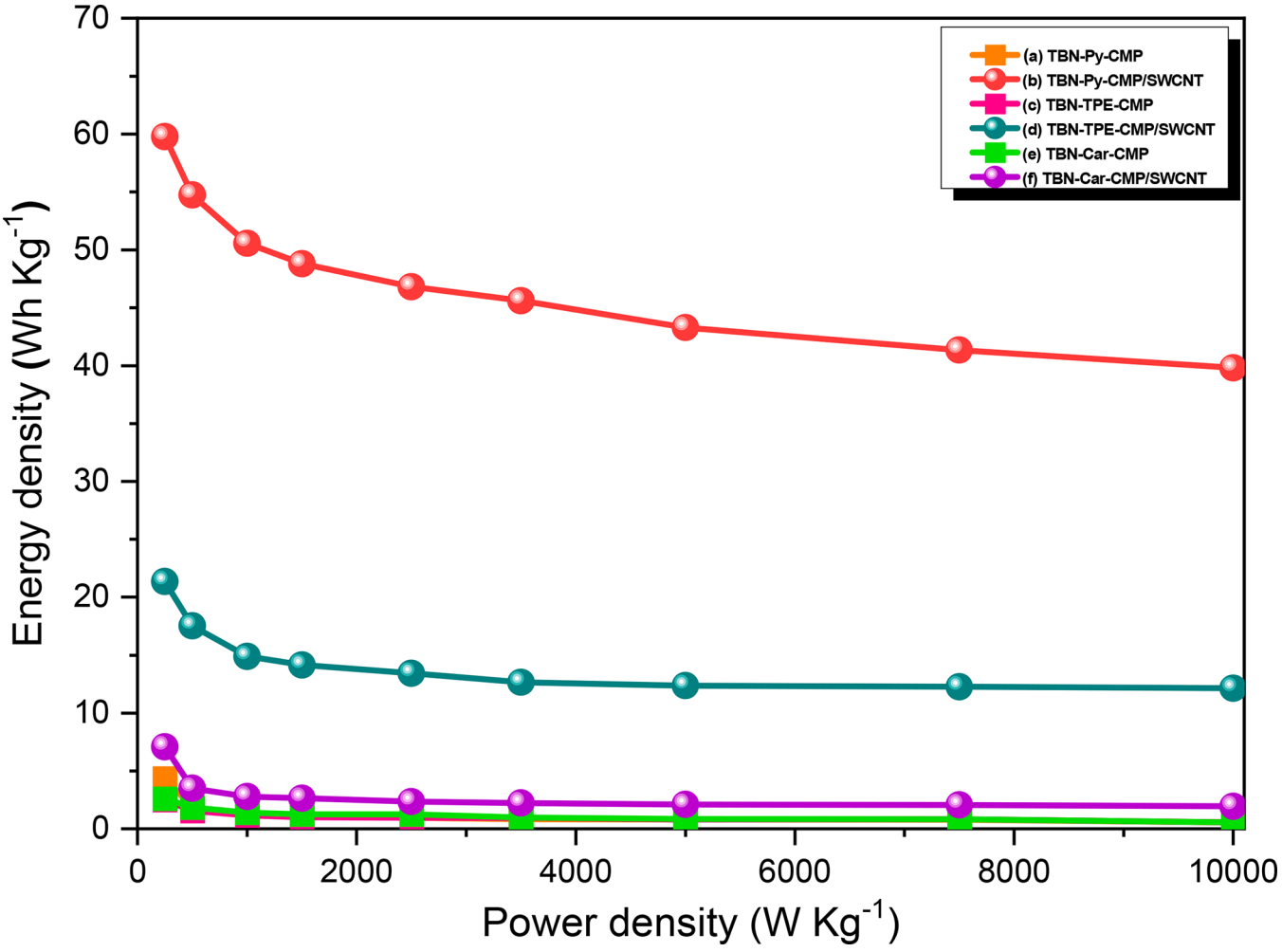

Figure 6. Ragone plots of (a) TBN−Py-CMP, (b) TBN−Py-CMP/SWCNT composite, (c) TBN−TPE-CMP, (d) TBN−TPE-CMP/SWCNT composite, (e) TBN−Car-CMP, and (f) TBN−Car-CMP/SWCNT composite electrodes in 1 M KOH.

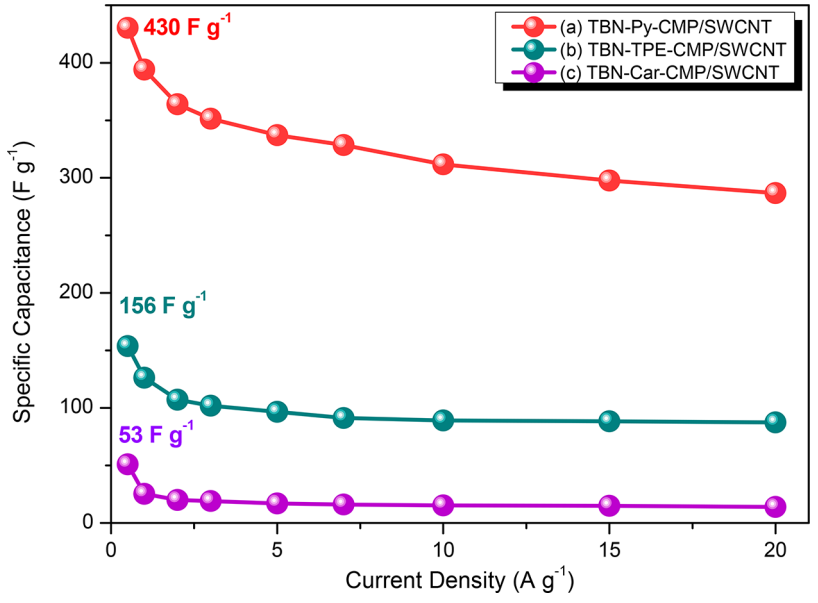

Figure 7. Specific capacitance profiles of the (a) TBN−Py-CMP/SWCNT, (b) TBN−TPE-CMP/SWCNT, and (c) TBN−Car-CMP/SWCNT composites, recorded at various current densities.

retentions of TBN−Py-CMP, TBN−TPE-CMP, and TBN−Car-CMP after 2000 cycles were 96.98, 95.21, and 96.86%, respectively; for the TBN−Py-CMP/SWCNT, TBN−TPE-CMP/SWCNT, and TBN−Car-CMP/SWCNT composites,

https://doi.org/10.1021/acsami.1c05720
ACS Appl. Mater. Interfaces XXXX, XXX, XXX−XXX

they were 99.18, 97.56, and 96.95%, respectively, revealing that both the cycling stability and capacitance retention improved after dispersion of the CMPs with the SWCNTs [Figures 4(f), 5(f), and S29(f)].

We recorded Ragone plots to evaluate the performance of the TBN-CMP supercapacitor electrodes before and after blending with the SWCNTs (Figure 6). The energy and power densities of the TBN-CMP/SWCNT composite electrodes were higher than those of the TBN-CMPs, due to the large surface area and high conductivity of the SWCNTs. Finally, the TBN−Py-CMP/SWCNT composite had a higher specific capacitance (430 F g^{-1}) and better capacitance retention (99.18%) after 2000 cycles when compared with the TBN−TPE-CMP/SWCNT and TBN−Car-CMP/SWCNT composites (Figure 7). We attribute the excellent energy storage performance of the TBN−Py-CMP/SWCNT composite to the strong π-stacking interactions between TBN−Py-CMP and the highly conductive SWCNTs. Table S2 summarizes the specific capacitances of TBN−Py-CMP, TBN−TPE-CMP, TBN−Car-CMP, TBN−Py-CMP/SWCNT, TBN−TPE-CMP/SWCNT, and TBN−Car-CMP/SWCNT compared to other porous materials. In this regard, Duan et al. reported a composite of cobalt phthalocyanine-linked conjugated microporous polymer hybridized with carbon nanotubes (CoPc-CMPs/CNTs) having capacitances of 365 and 289.1 F g^{-1} at 0.5 and 1 A g^{-1}, respectively.[52] In addition, Zhang et al. reported a CNTs@Mn-MOF composite exhibiting a capacitance of 203.1 F g^{-1} at 1 A g^{-1}.[57] Moreover, Lu et al. reported the synthesis of a GN/PPy/CNT composite, which showed a capacitance of 361 F g^{-1} at 0.2 A g^{-1}.[65] Gao and his group reported that hierarchical graphene/polypyrrole (GNS/PPy) nanosheet composites exhibited high capacitance of 318.6 F g^{-1} at 2 mV s^{-1}.[66] Furthermore, our group recently reported An-CPOP-1, An-CPOP-2, and DPT-HPP with capacitances of 72.75, 98.4, and 110 F g^{-1}, respectively, at 0.5 A g^{-1}.[6,47]

CONCLUSION

We have used Sonogashira coupling to prepare three new microporous conjugated polymers based on brominated TBN. TGA and BET measurements revealed that TBN−TPE-CMP possessed a high degradation temperature (505 °C), a high char yield (68%), a large surface area (1150 m^2 g^{-1}), and a high total pore volume (1.426 cm^3 g^{-1}) and featured pores of two sizes (1.04 and 2.00 nm). We blended our TBN-CMP materials with SWCNTs to prepare TBN-CMP/SWCNT nanocomposites for use as electrodes for supercapacitors. Among the three TBN-CMP/SWCNT composites, the TBN−Py-CMP/SWCNT electrode featured the highest specific capacitance (430 F g^{-1}) at 0.5 A g^{-1}, in addition to excellent capacitance retention (99.18%) over 2000 cycles at 10 A g^{-1}. We attribute the good performance of the TBN−Py-CMP/SWCNT supercapacitor electrode to the strong π-stacking between TBN−Py-CMP and the highly conductive SWCNTs.

ASSOCIATED CONTENT

Supporting Information

The Supporting Information is available free of charge at https://pubs.acs.org/doi/10.1021/acsami.1c05720.

Electrochemical procedures; synthetic scheme for monomer preparation and their characterizations; TGA analyses of TBN-CMP/SWCNT nanocomposites; electrochemical measurements of TBN−Car-CMP and TBN−Car-CMP/SWCNT; summaries of the specific capacitances of TBN−Py-CMP, TBN−TPE-CMP, TBN−Car-CMP, TBN−Py-CMP/SWCNT, TBN−TPE-CMP/SWCNT, and TBN−Car-CMP/SWCNT compared to other porous materials (PDF)

AUTHOR INFORMATION

Corresponding Authors

Kevin C.-W. Wu − *Department of Chemical Engineering, National Taiwan University, Taipei 10617, Taiwan; International Graduate Program of Molecular Science and Technology, National Taiwan University (NTU-MST), Taipei 10617, Taiwan;* orcid.org/0000-0003-0590-1396; Email: kevinwu@ntu.edu.tw

Shiao-Wei Kuo − *Department of Materials and Optoelectronic Science, Center of Crystal Research, National Sun Yat-Sen University, Kaohsiung 80424, Taiwan; Department of Medicinal and Applied Chemistry, Kaohsiung Medical University, Kaohsiung 807, Taiwan;* orcid.org/0000-0002-4306-7171; Email: kuosw@faculty.nsysu.edu.tw

Authors

Maha Mohamed Samy − *Department of Materials and Optoelectronic Science, Center of Crystal Research, National Sun Yat-Sen University, Kaohsiung 80424, Taiwan*

Mohamed Gamal Mohamed − *Department of Materials and Optoelectronic Science, Center of Crystal Research, National Sun Yat-Sen University, Kaohsiung 80424, Taiwan; Chemistry Department, Faculty of Science, Assiut University, Assiut 71516, Egypt;* orcid.org/0000-0003-0301-8372

Ahmed. F. M. EL-Mahdy − *Department of Materials and Optoelectronic Science, Center of Crystal Research, National Sun Yat-Sen University, Kaohsiung 80424, Taiwan*

Tharwat Hassan Mansoure − *Chemistry Department, Faculty of Science, Assiut University, Assiut 71516, Egypt;* orcid.org/0000-0002-5848-0196

Complete contact information is available at: https://pubs.acs.org/10.1021/acsami.1c05720

Author Contributions

#M.M.S. and M.G.M. contributed equally to the work and should be considered cofirst authors.

Notes

The authors declare no competing financial interest.

ACKNOWLEDGMENTS

This study was supported financially by the Ministry of Science and Technology, Taiwan, under contracts MOST 106-2221-E-110-067-MY3, 108-2638-E-002-003-MY2, and 108-2221-E-110-014-MY3. The authors thank the staff at National Sun Yat-sen University for assistance with TEM (ID: EM022600) experiments.

REFERENCES

(1) Yu, K.; Pan, X.; Zhang, G.; Liao, X.; Zhou, X.; Yan, M.; Xu, L.; Mai, L. Nanowires in Energy Storage Devices: Structures, Synthesis, and Applications. *Adv. Energy Mater.* **2018**, *8*, 1802369.

(2) EL-Mahdy, A. F. M.; Yu, T. C.; Mohamed, M. G.; Kuo, S. W. Secondary Structures of Polypeptide-Based Diblock Copolymers Influence the Microphase Separation of Templates for the Fabrication of Microporous Carbons. *Macromolecules* **2021**, *54*, 1030−1042.

(3) Simon, P.; Gogotsi, Y. Materials for Electrochemical Capacitors. *Nat. Mater.* **2008**, *7*, 845−854.

(4) Mohamed, M. G.; EL-Mahdy, A. F. M.; Ahmed, M. M. M.; Kuo, S. W. Direct Synthesis of Microporous Bicarbazole-Based Covalent Triazine Frameworks for High-Performance Energy Storage and Carbon Dioxide Uptake. *ChemPlusChem* **2019**, *84*, 1767−1774.
(5) Lin, Z.; Goikolea, E.; Balducci, A.; Naoi, K.; Taberna, P.L.; Salanne, M.; Yushin, G.; Simon, P. Materials for Supercapacitors: When Li-Ion Battery Power is not Enough. *Mater. Today* **2018**, *21*, 419−436.
(6) Mohamed, M. G.; EL-Mahdy, A. F. M.; Meng, T. S.; Samy, M. M.; Kuo, S. W. Multifunctional Hypercrosslinked Porous Organic Polymers Based on Tetraphenylethene and Triphenylamine Derivatives for High-Performance Dye Adsorption and Supercapacitor. *Polymers* **2020**, *12*, 2426.
(7) Mohamed, M. G.; Hung, W.-S.; EL-Mahdy, A. F. M.; Ahmed, M. M. M.; Dai, L.; Chen, T.; Kuo, S. W. High-Molecular-Weight PLA-b-PEO-b-PLA Triblock Copolymer Templated Large Mesoporous Carbons for Supercapacitors and CO_2 Capture. *Polymers* **2020**, *12*, 1193.
(8) Chen, D.; Jiang, K.; Huang, T.; Shen, G. Recent Advances in Fiber Supercapacitors: Materials, Device Configurations, and Applications. *Adv. Mater.* **2020**, *32*, 1901806.
(9) Young, C.; Park, T.; Yi, J. W.; Kim, J.; Hossain, M. S. A.; Kaneti, Y. V.; Yamauchi, Y. Advanced Functional Carbons and Their Hybrid Nanoarchitectures Towards Supercapacitor Applications. *ChemSusChem* **2018**, *11*, 3546−3558.
(10) Kim, J.; Kim, J. H.; Ariga, K. Redox-Active Polymers for Energy Storage Nanoarchitectonics. *Joule* **2017**, *1*, 739−768.
(11) Shi, R.; Han, C.; Duan, H.; Xu, L.; Zhou, D.; Li, H.; Li, J.; Kang, F.; Li, B.; Wang, G. Redox-Active Organic Sodium Anthraquinone-2-Sulfonate (AQS) Anchored on Reduced Graphene Oxide for High-Performance Supercapacitors. *Adv. Energy Mater.* **2018**, *8*, 1802088.
(12) Wulan Septiani, N. L.; Kaneti, Y. V.; Fathoni, K. B.; Wang, J.; Ide, Y.; Yuliarto, B.; Nugraha; Dipojono, H. K.; Nanjundan, A. K.; Golberg, D.; Bando, Y.; Yamauchi, Y. Self-Assembly of Nickel Phosphate-Based Nanotubes into Two-Dimensional Crumpled Sheet-Like Architectures for High-Performance Asymmetric Supercapacitors. *Nano Energy* **2020**, *67*, 104270.
(13) Kim, D.; Kang, J.; Yan, B.; Seong, K. D.; Piao, Y. Ambient Temperature Synthesis of Iron-Doped Porous Nickel Pyrophosphate Nanoparticles with Long-Term Chemical Stability for High-Performance Oxygen Evolution Reaction Catalysis and Supercapacitors. *ACS Sustainable Chem. Eng.* **2020**, *8*, 2843−2853.
(14) Wang, Y.; Li, W.; Zhang, L.; Zhang, X.; Tan, B.; Hao, J.; Zhang, J.; Wang, X.; Hu, Q.; Lu, X. Amorphous Cobalt Hydrogen Phosphate Nanosheets with Remarkable Electrochemical Performances as Advanced Electrode for Supercapacitors. *J. Power Sources* **2020**, *449*, 227487.
(15) Eftekhari, A.; Fang, B. Electrochemical Hydrogen Storage: Opportunities for Fuel Storage, Batteries, Fuel Cells, and Supercapacitors. *Int. J. Hydrogen Energy* **2017**, *42*, 25143−25165.
(16) Zhao, H.; Wang, J.; Zheng, Y.; Li, J.; Han, X.; He, G.; Du, Y. Organic Thiocarboxylate Electrodes for a Room-Temperature Sodium Ion Battery Delivering an Ultrahigh Capacity. *Angew. Chem., Int. Ed.* **2017**, *56*, 15334−15338.
(17) Schmidt, J.; Werner, M.; Thomas, A. Conjugated Microporous Polymer Networks via Yamamoto Polymerization. *Macromolecules* **2009**, *42*, 4426−4429.
(18) Weber, J.; Thomas, A. Toward Stable Interfaces in Conjugated Polymers: Microporous Poly(*p*-phenylene) and Poly(phenyleneethynylene) Based on a Spirobifluorene Building Block. *J. Am. Chem. Soc.* **2008**, *130*, 6334−6335.
(19) Fischer, S.; Schimanowitz, A.; Dawson, R.; Senkovska, I.; Kaskel, S.; Thomas, A. Cationic Microporous Polymer Networks by Polymerisation of Weakly Coordinating Cations with CO_2-Storage Ability. *J. Mater. Chem. A* **2014**, *2*, 11825−11829.
(20) Schmidt, J.; Weber, J.; Epping, J. D.; Antonietti, M.; Thomas, A. Microporous Conjugated Poly(thienylene arylene) Networks. *Adv. Mater.* **2009**, *21*, 702−705.
(21) Wang, H.; Cheng, Z.; Liao, Y.; Li, J.; Weber, J.; Thomas, A.; Faul, C. F. J. Conjugated Microporous Polycarbazole Networks as Precursors for Nitrogen-Enriched Microporous Carbons for CO_2 Storage and Electrochemical Capacitors. *Chem. Mater.* **2017**, *29*, 4885−4893.
(22) Jiang, J. X.; Su, F. B.; Trewin, A.; Wood, C. D.; Niu, H. J.; Jones, J. T. A.; Khimyak, Y. Z.; Cooper, A. I. Synthetic Control of the Pore Dimension and Surface Area in Conjugated Microporous Polymer and Copolymer Networks. *J. Am. Chem. Soc.* **2008**, *130*, 7710−7720.
(23) Vilela, F.; Zhang, K.; Antonietti, M. Conjugated Porous Polymers for Energy Applications. *Energy Environ. Sci.* **2012**, *5*, 7819−7832.
(24) Kou, Y.; Xu, Y.; Guo, Z.; Jiang, D. Supercapacitive Energy Storage and Electric Power Supply Using an Aza-Fused π-Conjugated Microporous Framework. *Angew. Chem., Int. Ed.* **2011**, *50*, 8753.
(25) Gu, C.; Huang, N.; Chen, Y.; Qin, L.; Xu, H.; Zhang, S.; Li, F.; Ma, Y.; Jiang, D. π-Conjugated Microporous Polymer Films: Designed Synthesis, Conducting Properties, and Photoenergy Conversions. *Angew. Chem., Int. Ed.* **2015**, *54*, 13594−13598.
(26) Zhang, C.; He, Y.; Mu, P.; Wang, X.; He, Q.; Chen, Y.; Zeng, J.; Wang, F.; Xu, Y.; Jiang, J.-X. Toward High Performance Thiophene-Containing Conjugated Microporous Polymer Anodes for Lithium-Ion Batteries through Structure Design. *Adv. Funct. Mater.* **2018**, *28*, 1705432.
(27) Zhu, J.; Yang, C.; Lu, C.; Zhang, F.; Yuan, Z.; Zhuang, X. Two-Dimensional Porous Polymers: From Sandwich-like Structure to Layered Skeleton. *Acc. Chem. Res.* **2018**, *51*, 3191−3202.
(28) EL-Mahdy, A. F. M.; Young, C.; Kim, J.; You, J.; Yamauchi, Y.; Kuo, S. W. Hollow Microspherical and Microtubular [3 + 3] Carbazole Based Covalent Organic Frameworks and Their Gas and Energy Storage Applications. *ACS Appl. Mater. Interfaces* **2019**, *11*, 9343−9354.
(29) EL-Mahdy, A. F. M.; Mohamed, M. G.; Mansoure, T. H.; Yu, H. H.; Chen, T.; Kuo, S. W. Ultrastable Tetraphenyl-*p*-Phenylenediamine-Based Covalent Organic Frameworks as Platforms for High-Performance Electrochemical Supercapacitors. *Chem. Commun.* **2019**, *55*, 14890−14893.
(30) Bezzu, C. G.; Carta, M.; Tonkins, A.; Jansen, J. C.; Bernardo, P.; Bazzarelli, F.; Mckeown, N. B. A spirobifluorene-Based Polymer of Intrinsic Microporosity with Improved Performance for Gas Separation. *Adv. Mater.* **2012**, *24*, 5930−5933.
(31) Du, N.; Park, H. B.; Robertson, G. P.; Dal-Cin, M. M.; Visser, T.; Scoles, L.; Guiver, M. D. Polymer Nanosieve Membranes for CO_2-Capture Applications. *Nat. Mater.* **2011**, *10*, 372−375.
(32) Zhang, W. J.; Tang, J. T.; Yu, W.; Huang, Q.; Fu, Y.; Kuang, G. C.; Pan, C. Y.; Yu, G. P. Visible Light-Driven C-3 Functionalization of Indoles over Conjugated Microporous Polymers. *ACS Catal.* **2018**, *8*, 8084−8091.
(33) Wang, B.; Xie, Z.; Li, Y.; Yang, Z.; Chen, L. Dual-Functional Conjugated Nanoporous Polymers for Efficient Organic Pollutants Treatment in Water: A Synergistic Strategy of Adsorption and Photocatalysis. *Macromolecules* **2018**, *51*, 3443−3449.
(34) Li, R.; Byun, J.; Huang, W.; Ayed, C.; Wang, L.; Zhang, K. A. I. Poly(benzothiadiazoles) and Their Derivatives as Heterogeneous Photocatalysts for Visible-Light-Driven Chemical Transformations. *ACS Catal.* **2018**, *8*, 4735−4750.
(35) Zhang, T.; Xing, G.; Chen, W.; Chen, L. Porous Organic Polymers: A Promising Platform for Efficient Photocatalysis. *Mater. Chem. Front* **2020**, *4*, 332−353.
(36) Mohamed, M. G.; Atayde, E. C.; Matsagar, B. M.; Na, J.; Yamauchi, Y.; Wu, K. C.-W.; Kuo, S.-W. Construction Hierarchically Mesoporous/Microporous Materials Based on Block Copolymer and Covalent Organic Framework. *J. Taiwan Inst. Chem. Eng.* **2020**, *112*, 180−192.
(37) Mohamed, M. G.; Liu, N. Y.; EL-Mahdy, A.F. M.; Kuo, S. W. Ultrastable Luminescent Hybrid Microporous Polymers Based on Polyhedral Oligomeric Silsesquioxane for CO_2 Uptake and Metal Ion Sensing. *Microporous Mesoporous Mater.* **2021**, *311*, 110695.
(38) Vyas, V. S.; Haase, F.; Stegbauer, L.; Savasci, G.; Podjaski, F.; Ochsenfeld, C.; Lotsch, B. V. A Tunable Azine Covalent Organic Framework Platform for Visible Light-Induced Hydrogen Generation. *Nat. Commun.* **2015**, *6*, 8508−8516.
(39) Aly, K. I.; Sayed, M. M.; Mohamed, M. G.; Kuo, S. W.; Younis, O. A Facile Synthetic Route and Dual Function of Network Luminescent

https://doi.org/10.1021/acsami.1c05720
ACS Appl. Mater. Interfaces XXXX, XXX, XXX−XXX

Porous Polyester and Copolyester Containing Porphyrin Moiety for Metal Ions Sensor and Dyes Adsorption. *Microporous Mesoporous Mater.* **2020**, *298*, 110063.
(40) EL-Mahdy, A. F. M.; Elewa, A. M.; Huang, S. W.; Chou, H. H.; Kuo, S. W. Dual-Function Fluorescent Covalent Organic Frameworks: HCl Sensing and Photocatalytic H_2 Evolution from Water. *Adv. Opt. Mater.* **2020**, *8*, 2000641.
(41) Mohamed, M. G.; Lee, C. C.; EL-Mahdy, A. F. M.; Luder, J.; Yu, M. H.; Li, Z.; Zhu, Z.; Chueh, C. C.; Kuo, S. W. Exploitation of Two-Dimensional Conjugated Covalent Organic Frameworks Based on Tetraphenylethylene with Bicarbazole and Pyrene Units and Applications in Perovskite Solar Cells. *J. Mater. Chem. A* **2020**, *8*, 11448−11459.
(42) Zhang, J.; Zhao, H.; Li, J.; Jin, H.; Yu, X.; Lei, Y.; Wang, S. In Situ Encapsulation of Iron Complex Nanoparticles into Biomass-Derived Heteroatom-Enriched Carbon Nanotubes for High-Performance Supercapacitors. *Adv. Energy Mater.* **2019**, *9*, 1803221.
(43) Deshagani, S.; Liu, X.; Wu, B.; Deepa, M. Nickel Cobaltite@ Poly(3,4-ethylenedioxypyrrole) and Carbon Nanofiber Interlayer Based Flexible Supercapacitor. *Nanoscale* **2019**, *11*, 2742−2756.
(44) Ma, H.; Li, C.; Zhang, M.; Hong, J. D.; Shi, G. Graphene Oxide Induced Hydrothermal Carbonization of Egg Proteins for High Performance Supercapacitors. *J. Mater. Chem. A* **2017**, *5*, 17040−17074.
(45) Deng, Y.; Xie, Y.; Zou, K.; Ji, X. Review on Recent Advances in Nitrogen-Doped Carbons: Preparations and Applications in Supercapacitors. *J. Mater. Chem. A* **2016**, *4*, 1144−1173.
(46) Mohamed, M. G.; Zhang, X.; Mansoure, T. H.; EL-Mahdy, A. F. M.; Huang, C. F.; Danko, M.; Xin, Z.; Kuo, S. W. Hypercrosslinked Porous Organic Polymers Based on Tetraphenylanthraquinone for CO_2 Uptake and High-Performance Supercapacitor. *Polymer* **2020**, *205*, 122857.
(47) Khattak, A. M.; Ghazi, Z. A.; Liang, B.; Khan, N. A.; Iqbal, A.; Li, L.; Tang, Z. A Redox-Active 2D Covalent Organic Framework with Pyridine Moieties Capable of Faradaic Energy Storage. *J. Mater. Chem. A* **2016**, *4*, 16312−16317.
(48) EL-Mahdy, A. F. M.; Kuo, C. H.; Alshehri, A. A.; Kim, J.; Young, C.; Yamauchi, Y.; Kuo, S. W. Strategic Design of Triphenylamine- and Triphenyltriazine-Based Two-Dimensional Covalent Organic Frameworks for CO_2 Uptake and Energy Storage. *J. Mater. Chem. A* **2018**, *6*, 19532−19541.
(49) Sengottaiyan, C.; Jayavel, R.; Shrestha, R. G.; Subramani, T.; Maji, S.; Kim, J. H.; Hill, J. P.; Ariga, K.; Shrestha, L. K. Indium Oxide/Carbon Nanotube/Reduced Graphene Oxide Ternary Nanocomposite with Enhanced Electrochemical Supercapacitance. *Bull. Chem. Soc. Jpn.* **2019**, *92*, 521−528.
(50) Samy, M. M.; Mohamed, M. G.; Kuo, S. W. Pyrene-Functionalized Tetraphenylethylene Polybenzoxazine for Dispersing Single-Walled Carbon Nanotubes and Energy Storage. *Compos. Sci. Technol.* **2020**, *199*, 108360.
(51) Li, J.; Lu, W.; Yan, Y.; Chou, T. W. High Performance Solid-State Flexible Supercapacitor Based on Fe_3O_4/Carbon Nanotube/Polyaniline Ternary Films. *J. Mater. Chem. A* **2017**, *5*, 11271−11277.
(52) Mei, L.; Cui, X.; Duan, Q.; Li, Y.; Lv, X.; Wang, H. G. Metal Phthalocyanine-Linked Conjugated Microporous Polymer Hybridized with Carbon Nanotubes as a High-Performance Flexible Electrode for Supercapacitors. *Int. J. Hydrogen Energy* **2020**, *45*, 22950−22958.
(53) Ran, F.; Yang, X.; Xu, X.; Bai, Y.; Shao, L. Boosting The Charge Storage of Layered Double Hydroxides Derived from Carbon Nanotube-Tailored Metal Organic Frameworks. *Electrochim. Acta* **2019**, *301*, 117−125.
(54) Han, Y.; Zhang, Q.; Hu, N.; Zhang, X.; Mai, Y.; Liu, J.; Hua, X.; Wei, H. Core-Shell Nanostructure of Single-Wall Carbon Nanotubes and Covalent Organic Frameworks for Supercapacitors. *Chin. Chem. Lett.* **2017**, *28*, 2269−2273.
(55) Zha, Z.; Xu, L.; Wang, Z.; Li, X.; Pan, Q.; Hu, P.; Lei, S. 3D Graphene Functionalized by Covalent Organic Framework Thin Film as Capacitive Electrode in Alkaline Media. *ACS Appl. Mater. Interfaces* **2015**, *7*, 17837−17843.
(56) Wang, D.; Min, Y.; Yu, Y.; Peng, B. A General Approach for Fabrication of Nitrogen-Doped Graphene Sheets and Its Application in Supercapacitors. *J. Colloid Interface Sci.* **2014**, *417*, 270−277.
(57) Zhang, Y.; Lin, B.; Sun, Y.; Zhang, X.; Yang, H.; Wang, J. Carbon Nanotubes@Metal−Organic Frameworks as Mn-Based Symmetrical Supercapacitor Electrodes for Enhanced Charge Storage. *RSC Adv.* **2015**, *5*, 58100−58106.
(58) EL-Mahdy, A. F. M.; Zakaria, M. B.; Wang, H. X.; Chen, T.; Yamauchi, Y.; Kuo, S. W. Heteroporous Bifluorenylidene-Based Covalent Organic Frameworks Displaying Exceptional Dye Adsorption Behavior and High Energy Storage. *J. Mater. Chem. A* **2020**, *8*, 25148−25155.
(59) Mohamed, M. G.; Tsai, M. Y.; Wang, C. F.; Huang, C. F.; Danko, M.; Dai, L.; Chen, T.; Kuo, S. W. Multifunctional Polyhedral Oligomeric Silsesquioxane (POSS) Based Hybrid Porous Materials for CO_2 Uptake and Iodine Adsorption. *Polymers* **2021**, *13*, 221.
(60) Venkataramana, G.; Sankararaman, S. Synthesis, Absorption, and Fluorescence-Emission Properties of 1,3,6,8-Tetraethynylpyrene and Its Derivatives. *Eur. J. Org. Chem.* **2005**, *2005*, 4162−4166.
(61) Mohamed, M. G.; Elsayed, M. H.; Elewa, A. M.; EL-Mahdy, A. F. M.; Yang, C. H.; Mohammed, A. K.; Chou, H. H.; Kuo, S. W. Pyrene-Containing Conjugated Organic Microporous Polymers for Photocatalytic Hydrogen Evolution from Water. *Catal. Sci. Technol.* **2021**, *11*, 2229−2241.
(62) Mohamed, M. G.; Ahmed, M. M. M.; Du, W. T.; Kuo, S. W. Meso/Microporous Carbons from Conjugated Hyper-Crosslinked Polymers Based on Tetraphenylethene for High-Performance CO_2 Capture and Supercapacitor. *Molecules* **2021**, *26*, 738.
(63) Su, C.; He, H.; Xu, L.; Zhao, K.; Zheng, C.; Zhang, C. A Mesoporous Conjugated Polymer Based on a High Free Radical Density Polytriphenylamine Derivative: Its Preparation and Electrochemical Performance as A Cathode Material for Li-Ion Batteries. *J. Mater. Chem. A* **2017**, *5*, 2701−2709.
(64) Li, Z.; Zhang, W.; Li, Y.; Wang, H.; Qin, Z. Activated Pyrene Decorated Graphene with Enhanced Performance for Electrochemical Energy Storage. *Chem. Eng. J.* **2018**, *334*, 845−854.
(65) Lu, X. J.; Zhang, F.; Dou, H.; Yuan, C. Z.; Yang, S. D.; Hao, L.; Shen, L. F.; Zhang, L. J.; Zhang, X. G. Preparation and Electrochemical Capacitance of Hierarchical Graphene/Polypyrrole/Carbon Nanotube Ternary Composites. *Electrochim. Acta* **2012**, *69*, 160−166.
(66) Xu, C.; Sun, J.; Gao, L. Synthesis of Novel Hierarchical Graphene/Polypyrrole Nanosheet Composites and Their Superior Electrochemical Performance. *J. Mater. Chem.* **2011**, *21*, 11253−11258.

https://doi.org/10.1021/acsami.1c05720
ACS Appl. Mater. Interfaces XXXX, XXX, XXX−XXX